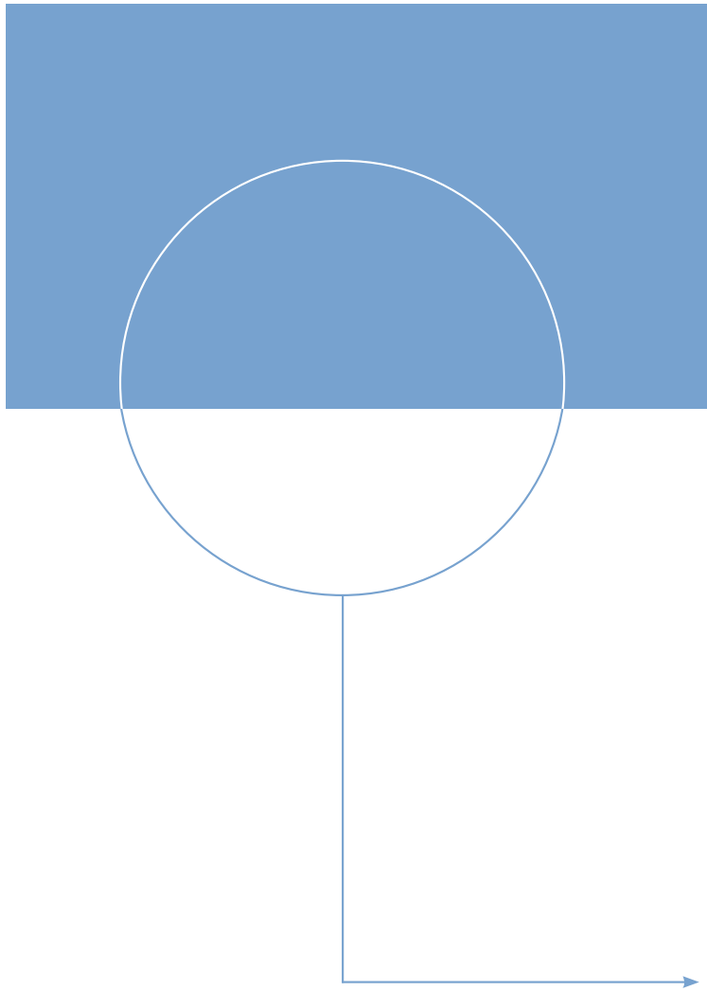

Master's thesis

2022

Mughal Andleeb

NTNU
Norwegian University of
Science and Technology
Faculty of Engineering
Department of Geoscience and Petroleum

Mughal Andleeb

Modelling acoustic pressure of very shallow airguns

August 2022

NTNU
Norwegian University of
Science and Technology

NTNU
Norwegian University of
Science and Technology

NTNU
Norwegian University of
Science and Technology

Modelling acoustic pressure of very shallow airguns

Mughal Andleeb

MSc Petroleum Geoscience
Submission date: August 2022
Supervisor: Børge Arntsen
Co-supervisor: Martin Landrø

Norwegian University of Science and Technology
Department of Geoscience and Petroleum

Abstract

A surge of advancements in air-gun technologies propels geophysicists to ask the uncomfortable question. Is there an alternative to equipment-based low-frequency enhancement? Most marine seismic acquisition setups are inclined towards deep-towed air-gun placement to acquire a broadband pressure response. Such surveys combine multiple sources to reduce subsequent bubble oscillations after the first peak and the shot effect that directly reduces the frequency bandwidth of the signal. These methods modify the acquired signal into an ideal signature.

This thesis aims to model the acoustic pressure response of sources placed very close to the free surface to understand the contribution of bubble energy toward low-frequency band enhancement. The modelled data is compared against the recorded data from a water tank experiment conducted for sources placed at 0.1 m and 0.15 m, and an offshore experiment at a source depth of 7.5 m below the free surface. The modelled pressure response matched well with the recorded data from the water tank experiments. The modelling approach accounts for the interaction of bubble and free surface by modifying parameters in the Rayleigh-Plesset equation such as dynamic viscosity of the medium and the polytropic constant. The modelling is performed in two stages;

1) The bubble radius is modelled until the equilibrium state after the critical radius is reached i.e when the bubble breaks the thin water layer and is contracting.

2) Initial velocity and radius are redefined for sources placed deeper than 0.1 m to model the bubble oscillations after bubble and free surface interaction.

The displacement of the free surface is estimated from the modelled radius and compared against the expected value. The pressure response of the bubble is used to estimate the near-field and far-field signal at a receiver depth of 0.5 m and 20 m respectively. The frequency spectrum of the far-field pressure signal is normalised and compared against the spectrum of recorded pressure response at 7.5 m source depth to observe the relative change in the amplitude of the frequency spectrum. The comparison shows an increase in 7.6 dB in amplitude for frequencies between 0-12 Hz at 0.15 m source depth and an increase in 6.6 dB in amplitude for frequencies between 0-7 Hz at 0.1 m source depth. This increase in the low-frequency amplitude spectrum can aid in mitigating cycle skipping issues in Full Waveform Inversion.

Contents

Figures

Tables

Chapter 1

Introduction

On a summer day in 1921, a team of physicists and geologists performed the first seismic survey, with a handful of equipment consisting of a dynamite charge as the seismic source and a seismograph as the receiver (Dragoset, 2005). Since then, Seismic exploration has come a long way in terms of development in source and receiver technology as well as an understanding of the factors affecting the recorded seismic signal.

In the early developing days of marine seismic exploration, from 1940 to the 1950s, dynamite and similar sources were used conventionally. Since then, there has been a steady development of marine seismic sources in designing the ideal source signature. Compared to dynamite sources, pneumatic sources called 'air-guns', introduced in the 1960s were significantly safer and more environmentally friendly than the former source type (Dragoset, 2005). The air guns were designed to simulate the signature of the dynamite source by utilizing high-pressure air operating at a certain volume (ex. 200 bar) that controls the initial radius of the oscillating bubble. The high-pressure air is activated and released into the surrounding water by a piston with a certain acceleration distance to produce a bubble that generates a pressure signal as it oscillates. The bubble period contributes toward the enhancement of low frequencies - as a longer bubble period equates to a lower fundamental frequency (Hegna and Parkes, 2012). The bubble oscillations after the first peak are removed in the seismic data processing workflow via de-bubbling which removes low-frequency information from the pressure signal which is important for velocity model building and in mitigating cycle skipping issues for FWI.

Near-field pressure signals recorded in the water tank experiments conducted by Wehner (2019a) are devoid of bubble oscillations and source ghosts at 10 cm source depth and have higher low-frequency amplitude spectra. This is likely a result of the change in reflection coefficient as the bubble expands beyond the surface, breaks and collapses instantly. Several authors have studied bubble motion near an interface for different air bubble sizes. T. Li et al. (2019) compared bursting and non-bursting cases for bubbles near a free surface and suggested gas flow as a factor affecting the bubble bursting behaviour. Cui et al.

(2016) studied underwater explosions near one or two boundaries such as a free surface and a solid boundary through high-speed photographs captured from an experiment. Krieger and Chahine (2005) discussed the acoustic signal generated by small bubbles near an interface created by the discharge between two electrodes. H. N. and A (1990) demonstrated a numerical model for bubble oscillations near a plane-free surface. Haavik (2016) studied the changes in the bubble period when an airgun is placed close to the free surface.

Other authors examine the behaviour of bursting bubbles and changes in their internal volume and pressure. Boulton-Stone and Blake (1993) modelled a bursting gas bubble and the energy released from it. Loo et al. (2012) studied the collapse of cavitating bubbles through numerical modelling with variation in Reynold's number. The studies conclude that the reduction in oscillations of a bursting gas bubble depends on the effective viscosity of the surrounding medium as it changes from water to air. This viscosity is measured as a function of the medium density and is analogous to the velocity at the bubble wall.

Recent developments in pneumatic sources have been made in terms of design and frequency bandwidth such as the Tuned Pulse Source (TPS) that can lessen the effect of ghost cavitation - the shadow of the ghost signal. A study performed by Long (2021) suggests an 18% increase in the time bubble period which is an indication of increased amplitude in the low-frequency part of the signal spectrum caused by a modification in the airgun design. This effect is also seen in airguns placed very shallow to the free surface (Amundsen and Landro, 2014). Many other factors affect the low-frequency amplitude of the airgun's pressure signal; ghost cavitation (Khodabandeloo and Landrø, 2017), source ghost (Sanders and Barr, 1989), shot effect (Hatton and Parkes, 1986), and the change in reflection coefficient of the free surface Hatton (2007). Source depth is also a contributing factor as at shallow depths the collapse of the oscillating air bubble contributes toward the enhanced low-frequency amplitudes (Mayne and Quay, 1971).

By modelling the pressure response from shallow sources, this thesis aims to understand the factors contributing toward reduced bubble oscillations and source ghost as observed in experiments conducted by Wehner (2019a). The following chapters in this thesis describe the theory, modelling methodology and results. Chapter 2 gives the reader an understanding of an airgun signature and the factors affecting it. Chapter 3 is a description of the Rayleigh-Plesset modelling, dampening terms, and the conversion of near field signal into far-field signal. Chapter 4 will present the modelling scheme developed to investigate the interactions between a shallow source-generated bubble with the free surface. Chapters 5 and 6 build on chapter 4 and present the results and discussion with the conclusion and future recommendations regarding the modelling approach described in this thesis.

Chapter 2

Theory

Marine seismic acquisition methods are similar theoretically to land-based seismic surveys. They both have a source that generates sound waves and a receiver that records pressure disturbance caused by reflected and refracted sound waves from the source. However, they differ in their field equipment and the technique of survey and geographic control. Marine surveys have a towed transmitter and an array of geophones as receivers. Different types of marine sources exist for different kinds of marine applications such as marine vibrators (5-100 Hz) (PGS, 2017), water guns (20-1500 Hz), air Gun (100-1500 Hz), boomers (300-3000 Hz), sparkers (50-4000 Hz) to acquire deeper seismic data and chirp Systems (500 Hz-12 kHz, 2-7 kHz, 4-24 kHz, 3.5 kHz, and 200 kHz) to acquire high resolution shallow seismic data (U.S. Environmental Protection Agency, 2016).

In the following section observed effects of placing airguns very close to the free surface are described along with the field and water tank experiments that will be used to compare the modelled data.

2.1 Shallow Sources

As stated in the introduction, an airgun is a device that expels compressed air into the surrounding water giving rise to an air-filled bubble with an initial radius that is proportional to the depth of the source and the initial volume of compressed gas in the source's chamber. After the firing pressure drops, the bubble tends to oscillate at a specific resonance frequency. The pressure response of the airgun at shallow depths as seen in Wehner (2019a) is different from that recorded for source placed deeper, in experiments conducted by Amundsen et al. (2017). At shallow sources, the signal is nearly devoid of a source ghost and has a relatively higher peak to bubble ratio. This can partly be attributed to the change in reflection coefficient at the free surface which is taken as -1 for the difference in impedance response between water and air. However, in the case of near-surface airgun explosion, the reflection coeffi-

cient is likely to be greater than -1. For comparison, Kryvohuz and Campman (2018) suggest a difference of 30% in reflection coefficient for a 100 Hz signal propagating at normal incidence to the free surface when the sea surface roughness coefficient (σ) is taken into account.

2.1.1 Reduced Source Ghost and Bubble Oscillations

A seismic airgun signature is characterized by its peak signal energy, bubble energy, and the source ghost. The pressure signal produced by the source propagates in all directions. The downward propagating signal is recorded by a hydrophone placed right below the source, this is the notional source signature. The upward propagating signal interacts with the water-air interface and is reflected down with a negative reflection coefficient towards the hydrophone where it is recorded.

The peak source signature amplitude attenuates with increasing depth, and at shallow depths, the pressure wavefield from the source will interact with the free surface with a higher incident amplitude compared to sources placed deeper (Loveridge, 1985). A study conducted by Kryvohuz and Campman (2018) models the frequency-dependent reflection coefficient of a near-field pressure signal. The true reflection coefficient is derived from the notional source and is -1 at low frequencies while it increases linearly for higher frequencies. The effect of change in reflection coefficient for airgun signals is noticeable for frequencies above 80Hz. The effective reflection coefficient that is dependent on the sea surface roughness parameter σ and the angle of incidence at the sea surface ($cos\theta$) is given as (Kryvohuz and Campman, 2018):

$$r_{eff} = -exp(-2(\sigma\omega cos\theta/c)^2) \tag{2.1}$$

Where ω is the angular frequency and θ is the angle of incidence of the pressure signal to the free surface, and c is the velocity of sound in the medium, in this case, water ($c = 1450m/s^2$). Hatton (2007) derived a novel equation for the reflection coefficient as a function of source depth relative to the free surface from recorded data as:

$$r_h = 1.3\left(\frac{P_p}{z_s^2}\right)^{\frac{1}{5}} - 1.7 \tag{2.2}$$

Here, z_s is the source depth expressed in meters and P_p is the zero to peak pressure expressed in bar-m. The modified equation for the ghost function is given as (Zhou and Amundsen, 2013):

$$|G(\omega)| = |(1 + r_h \exp(-i2\omega z_s/c))| \tag{2.3}$$

The reflection coefficient will only vary if the incident pressure wavefield p interacts with the free surface at a critical acoustic pressure (p_c). This pressure will vary in the presence of free surface waves (i.e. surface disturbance)

and environmental effects such as weather. If external factors are ignored, the critical pressure and bubble radius required to break the free surface and its corresponding critical distance (r_c) as described by Loveridge (1985) and Weston (1960) are:

$$p_c = \frac{1}{2}\sum_{j=1}^{2}\frac{1}{N}\sum_{m=1}^{N} max(p_{i,n})\left(\frac{r_i}{r_c^m}\right), r_c = \sqrt{d^2 + z_s^2} \tag{2.4}$$

Where $max(p_{i,n})$ is the maximum pressure measured at the shot number (n) and receiver number (i). N is the number of recorded signals, and r_i is the source-receiver distance, d is the radius of the disturbed surface and z_s is the source depth. The constant $m = 1, 2$ takes into account the linear and quadratic spreading correction, and hence r_c^m is the critical radius scaled by m. At small source-receiver distances when the difference between r_i and r_c^m is small, the difference in critical pressure due to linear and/or quadratic spreading correction is also small.

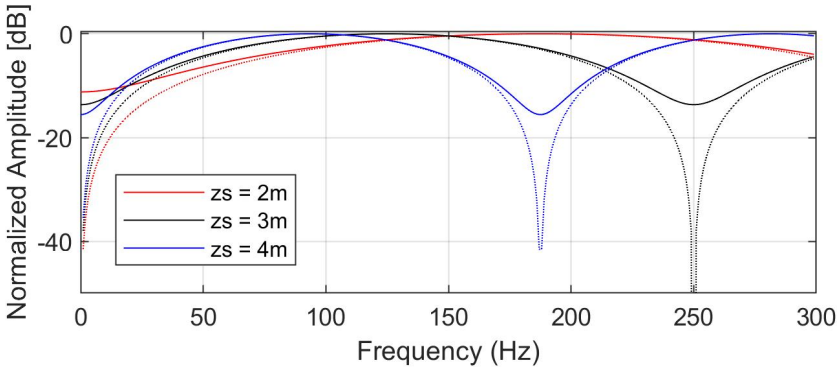

Figure 2.1: Frequency spectra of ghost reflections at varying source depths. Solid lines represent modelled ghost reflection by using Eq. 2.2 and Eq. 2.3. Dashed lines represent modelled ghost reflection using Eq. 2.3 with a reflection coefficient of -1 at the free surface.

The reduced ghost reflection in figure 2.1 represented by the dotted line is derived using Eq. 2.3 and results in smoother notches (Wehner, 2019a) that can aid in preserving the lower and higher frequencies in the recorded source signature and seismic data. At high zero to peak pressure values, the reflection coefficient can result in high positive values which is unrealistic when the difference in the density of gas inside the bubble and the density of air is much less, resulting in a similar impedance value for air-gun gas-water and air-water interfaces. The shot effect is observed at high zero to peak pressure values such as in the shallow source depth recordings presented by Wehner (2019a). This shot effect is the likely cause of higher low-frequency amplitudes at shallow source depths.

2.1.2 Bubble Oscillation

A cavity/bubble is generated when the compressed air from the airgun is suddenly released into the surrounding water (Hatton and Parkes, 1986). When the radius of the bubble is at its minimum, the pressure inside the bubble is far greater than the hydrostatic pressure. The bubble expands to its maximum radius and the pressure inside the bubble becomes equal to the hydrostatic pressure. The bubble radius will achieve an equilibrium state after which it will start decreasing, and at this point, the pressure inside the bubble is much less than the hydrostatic pressure. The collapse of the bubble exceeds the equilibrium position and the bubble continues to oscillate for a period in the range of tens of hundreds of milliseconds. Through oscillation, a bubble loses higher frequencies that contribute toward notches in the frequency spectrum of the signal. These notches occur at the following frequencies, where τ is the bubble period, and n is the number or oscillation (Amundsen and Landro, 2014):

$$f_b = \frac{n + \frac{1}{2}}{\tau}, n = 0, 1, 2.... \tag{2.5}$$

The oscillating bubble breaks due to buoyancy which is the displacement of the fluid caused by the gas bubble. If the bubble oscillation is stopped after the initial peak then the signature will result in a spike with reduced bubble energy. Figure 4.5 in Wehner (2019a) shows a reduced bubble amplitude for airguns placed at shallow source depths. The reduced bubble amplitude can be attributed to the interaction of the growing bubble with the free surface upon which it collapses instantly. The depth at which an airgun bubble can interact with the free surface depends on the charge weight taken as the volume of the airgun in inch^3, while 3.8 is an empirical constant in the equation given as (Sheriff, 2002):

$$d_{fs} = 3.8 V_g^{1/3} \tag{2.6}$$

In the water tank experiments, the signal recorded in the air is 300-400 times weaker than the signal recorded in water for frequencies below 300Hz. The contribution of the acoustic signal recorded in the air comes from two sources; sound waves emitted from the moving water surface and the signal released in the air through the breaking of the water surface. The resultant air signal has weaker lower frequency amplitudes and stronger higher frequency amplitudes. The number of oscillations a bubble goes through depends on how quickly the pressure of the gas inside the bubble reaches equilibrium relative to the pressure of the surrounding medium. The camera recordings of this experiment show the generation of a jet which follows the modelled change in pressure and radius of the oscillating bubble bursting at the free surface as described by T. Li et al. (2019).

2.1.3 Bubble Time Period

A bubble period is defined as the time taken from the first prominent peak (primary) to the second prominent peak (bubble) of a source signature. The primary to bubble ratio is equivalent to signal to noise ratio and must be as large as possible. To understand the relation between bubble period and source depth, we will look at the Rayleigh-Willis (1941) equation which is given as:

$$T_{rw} = C\frac{P_f^{\frac{1}{3}} V_g^{\frac{1}{3}}}{p_h^{\frac{5}{6}}} \tag{2.7}$$

Here, C is a constant specific to the airgun design, P_f is the firing pressure, V_g is the volume of the airgun and p_h is the hydrostatic pressure.

This equation is a modified version of the equation derived by Rayleigh (1917) which describes the motion of an oscillating bubble in an incompressible, inviscid and infinite medium. The equation modified by Willis (1941) doesn't consider the effects of the free surface.

This equation is modified for the case where the bubble is very close to the free surface and is given as (Haavik, 2016):

$$T_{hl} = T_{rw}\frac{1}{2}\sqrt{A_{(k,r)}} \tag{2.8}$$

where:

$$A_{(k,r)} = \frac{4k + 4r - r^2 \ln\left(\frac{k-1}{k+1}\right)}{k} + \frac{2r^2}{1-k^2}, k \geq 4 \tag{2.9}$$

where, $k = 2z_s/R_{eq}$, r is the reflection coefficient of the free surface, z_s is the source depth from the free surface (-1), R_{eq} is the equilibrium bubble radius; when the pressure inside the bubble is equal to the pressure outside the bubble. The equilibrium radius for a bubble close to the free surface will be the radius at which the bubble bursts r_c, as during that event the gas inside the bubble escapes into the atmosphere and the pressure inside the bubble will reach equilibrium quickly.

2.1.4 Surface Displacement

Oscillating bubbles generated by shallow sources may expand beyond the level of the free surface thus generating a net surface displacement denoted by h in figure 2.2. The bubble expansion depends on the initial air gun pressure and the source depth. At lower airgun pressures, the mass flow rate is low and the bubble oscillation period is reduced. At shallow source depths, the bubble quickly expands as the mass flow rate is high. The rising bubble expands the surface until the critical radius 2.4 is reached and the bubble collapses. The following equation for surface displacement validates the ad-hoc model as presented

in Krieger and Chahine (1977) and Wehner (2019a). This surface displacement h_{ch} is related to the distance between the free surface and the centre of the bubble (r_{b-fs}) for a given bubble radius R and is given as (Krieger and Chahine, 2005):

$$h_{ch} = \frac{2}{\left(r_{b-fs}^2 + 1\right)^{\frac{3}{2}}} \frac{4}{3}\pi R^3 \tag{2.10}$$

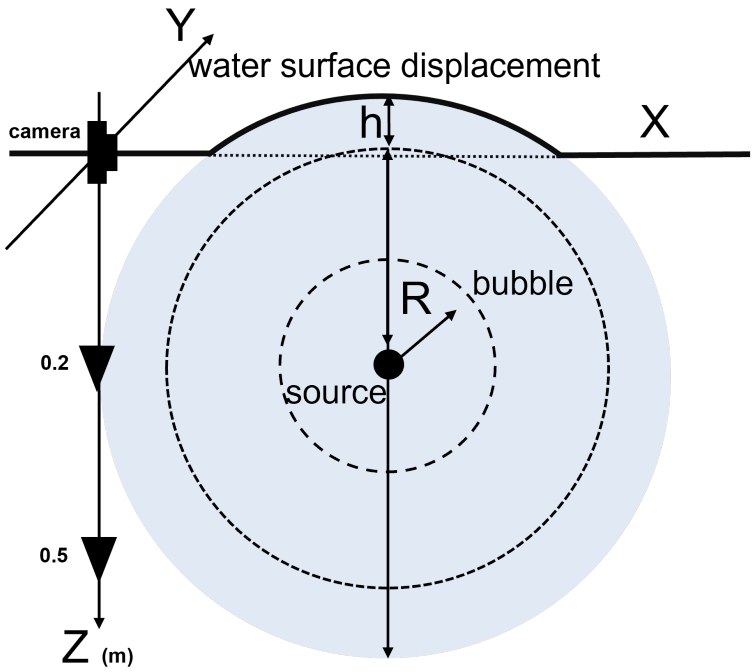

Figure 2.2: Modified sketch of the free surface displacement h caused by the airgun bubble, as illustrated in Wehner (2019a).

Depending on the source firing pressure and depth, the maximum achievable bubble radius can be calculated using Eq. 2.4. At the same time, the bubble is kept intact by a thin water layer which in theory will break if the bubble reaches a radius that is higher than the critical radius. However, in experiments conducted for sources placed at 0.1 and 0.3m, the surface displacement stays constant after the critical radius is achieved (Wehner Daniel and Lasse). This observation is also demonstrated in Robinson et al. (2001) of nearly stationary surface displacement during a collapsing cavity. This surface displacement is illustrated in figure 2.2.

2.2 Primary Bjerknes Force

If an external acoustic force acts on a bubble with a non-zero pressure differential, it can couple itself with the bubble oscillations to produce a translational force on the bubble that is referred to as the primary Bjerknes force. This force can be described as "forced oscillation on a resonance system" and is given as (Leighton et al., 1989):

$$F_b = -V_b(t)\Delta p(z,t) \tag{2.11}$$

Where V_b is the volume of the bubble and Δp is the radiating pressure from the bubble.

2.3 Field Experiment

Figure 2.3 presents an illustration of the acquisition setup of the data acquired from a field test which was carried out in the Norwegian Fjord (Amundsen et al., 2017). At the test site, the water depth was 390m and the weather conditions throughout the test were good. The experiment used a single Bolt1500LL airgun with a 1200inch^3 volume which was positioned by an A5 buoy and was fired at varying source depths below the water surface. The pressure response was recorded on a Reson TC4043 hydrophone located at 80m below the source. The hydrophone was kept nearly vertical throughout the experiment by attaching a weight to it. The x-coordinate of the hydrophone is an estimate and might slightly vary. The recommended frequency range of the hydrophone is from 2 Hz to 160 kHz. The pressure response was acquired at source depths = 1.3, 2.3, 3.3, 5.3, 7.3, 10.3, 20.3, and 30.3 m with an additional shot between 1.3 m and 2.3 m. As the airgun was lowered due to a leakage in the A5 buoy, source depths are uncertain. The experiment only recorded one shot at 1.3 m as the experiment was designed for deeper sources. A more detailed description is provided in Amundsen et al. (2017).

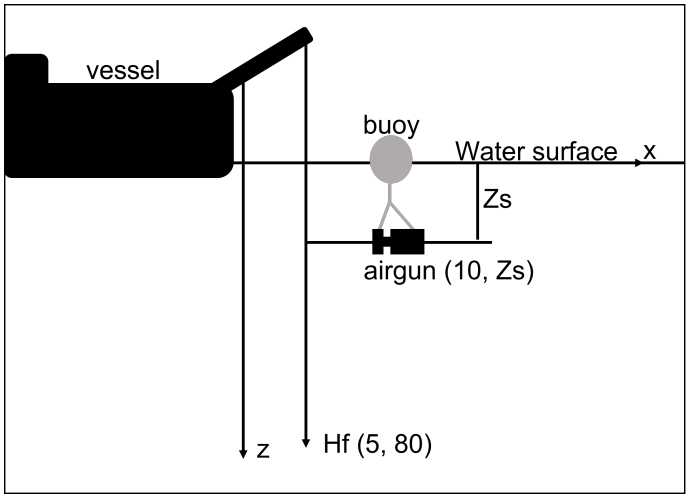

Figure 2.3: Modified sketch of field experiment performed in the Norwegian Fjord, taken from Amundsen et al. (2017). Hf is the hydrophone given with its respective x- and z-coordinate in meters and the water when experimenting was recorded as 390m deep.

2.4 Water Tank Experiment

The water tank experiment is illustrated in figure 2.4 with its dimensions. The water tank setup was bounded by 5cm thick foam mattresses that act as damping material and enhance signal reception but contain small side reflections and are not perfectly absorbing boundaries. The reference data taken for comparison with modelled data are source signatures acquired in a water tank with a Mini G Gun fired with an operating volume of 12 inch^3. The data was acquired at depths ranging from 0.8m to 0.1m. The hydrophones used for this experiment are Brüel and Kjær type 8105 which have a frequency range of 0.1 Hz to 100 kHz. The hydrophone H3 is placed in the air to record the transmitted signal through the free surface. Cameras 1 and 2 are placed in air and on the water surface to record the water surface as the source is fired at varying depths. The cameras have a recording rate of 240 frames per second (fps) that allow a photo to be captured every 4.2ms. These recordings are used to determine the surface displacement at the air-water interface. To ascertain the impact of tank size on the recorded signals, the non-repeatability of the experiment for an average number of 10 shots per source depth that has been low-pass filtered at 300Hz was found to be $\leq$ 5%. A more detailed description is provided in Wehner (2019a).

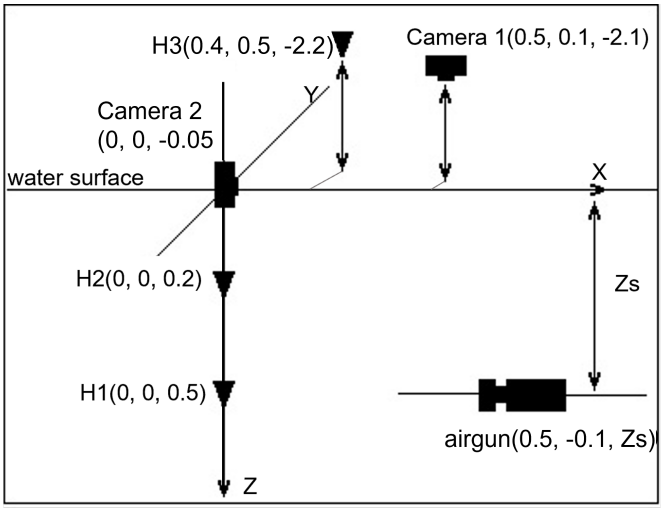

Figure 2.4: Modified sketch of experimental water tank setup, taken from Wehner (2019a). H1, H2 and H3 are hydrophones given with their respective x-, y-, and z-coordinates in meters. The depth, width and length of the tank are 1.25m, 2.5m and 6m, respectively.

Chapter 3

Acoustic Pressure of a Seismic Source

3.1 Simple Acoustic Pressure Modelling

Bubble oscillations in an incompressible fluid are a phenomenon that affects several disciplines such as ultrasound, marine seismic, and ocean engineering. Besant (1859) derived an equation for the period required to fill a cavity neglecting surface tension and viscosity. Considering variable pressure inside the bubble, this equation was modified through integration by Lord Rayleigh (1917). Plesset (1949) included the effects of surface tension and applied the equation to cavitation bubbles. The equation makes restrictive assumptions regarding the expansion of the bubble. It assumes that the fluid surrounding the cavity is incompressible, the bubble wall velocity is small compared to the speed of sound, and the pressure differential for time is very small. Moreover, the original Rayleigh-Plesset equation does not include any energy radiation losses as the sound would not propagate in an incompressible fluid. These assumptions are valid for bubble motion and expansion in an ideal environment but are invalid for air-gun bubble modelling where energy dissipation plays an important role. Several models have been derived from the Rayleigh equation that consider the physical effects on bubble motion such as surface tension, viscosity, and acoustic dissipation (Plesset and Prosperetti, 1977; Gilmore, 1952; Kirkwood and Bethe, 1942; Keller and Kolodner, 1956).

For a bubble oscillating in an infinite incompressible medium such as water, we calculate the ambient pressure at source depth z_s by adding the atmospheric pressure (P_{atm}) to hydrostatic pressure p_∞:

$$p_\infty = P_{atm} + \rho g z_s \tag{3.1}$$

The density of the surrounding medium ρ is kept constant as the compressibility of the medium is important in the event of a collapse, g is the gravitational constant. The difference between p_∞ and the scattered pressure

from the bubble, $p(t)$, controls the maximum radius for a given initial radius R_o (Ziolkowski, 1970).

$$p(t) = p_0 \left(\frac{R_0}{R} \right)^{3\gamma} \tag{3.2}$$

Here, p_0 is the initial pressure inside the bubble taken as the operating pressure of the airgun, γ is the polytropic index that varies between 1.4 for an adiabatic system and 1 for an isothermal system. However, the heat capacity of the gas "for most airguns" was estimated to be around 1.13 by Ziolkowski (1970) which is the value used in this modelling. The parameter airgun volume (V_g) controls the initial radius of the bubble R_0 as (Ziolkowski, 1970):

$$R_0 = \left(\frac{3V_g}{4\pi} \right)^{\frac{1}{3}} \tag{3.3}$$

The scattered pressure $p(t)$ can be evaluated by solving a second order non-linear differential equation that describes the radiating bubble motion $\ddot{R}$ (Rayleigh, 1917) that is:

$$R\ddot{R} + \frac{3}{2}\dot{R}^2 = \frac{p(t) - p_\infty}{\rho} \tag{3.4}$$

Where R is the radius of the oscillating bubble, and $\dot{R}$ and $\ddot{R}$ are velocity and acceleration taken as first and second-order differentials of the bubble radius (R), respectively. We see that the particle velocity is zero for the maximum bubble radius. Rayleigh equation has been improved on by many authors, one of which is the modified Herring equation given as (Vokurka, 1986; Herring, 1941):

$$R\ddot{R} + \frac{3}{2}\dot{R}^2 = \frac{p(t) - p_\infty}{\rho} + \frac{R\dot{p}}{\rho c} \tag{3.5}$$

The last term on the right side allows energy loss through acoustic radiation within the medium, where $\dot{p(t)}$ is the first order differential of pressure inside the bubble presented in its non-dimensional form (Hoff, 2003):

$$\dot{p(t)} = 3\gamma(1 + l + \epsilon)^{-3\gamma-1}, l = \frac{R - R_0}{R_0} \tag{3.6}$$

ϵ is added to avoid infinities and has a value of 0.001.

Equation 3.5 does not account for attenuation in oscillations due to surface tension and viscosity. The modified Rayleigh-Plesset equation is given as (Brennen, 2013):

$$\ddot{R} = \frac{p(t) - p_\infty}{\rho R} - \frac{3}{2}\frac{\dot{R}^2}{R} - \frac{4\nu_w \dot{R}}{ReR^2} - \frac{2S}{\rho R^2}\left(\left(\frac{R_0}{R} \right)^{3\gamma} - 1 \right) + \frac{R\dot{p(t)}}{\rho c} \tag{3.7}$$

v_w is the viscosity constant for water taken as $0.01/\rho$, S is the surface tension of water, and the Reynolds number (R_e) accounts for the change in gas density inside the bubble as (Loo et al., 2012):

$$Re = \sqrt{\frac{SR}{\rho \dot{R}^2}} \tag{3.8}$$

Here, ρ is taken as 1000 Kg/m^3 for water and 1.3 Kg/m^3 for air.

By numerically integrating Eq. 3.7 through an ODE solver we can find the radius and particle velocity at the bubble wall.

3.2 Acoustic Pressure Recorded at the Receiver

The acoustic pressure radiating from an oscillating bubble recorded at a receiver point is given as (Gilmore, 1952):

$$p_n(t) = \rho_\infty \frac{R}{r_i}\left(H + \frac{(r_i^3 - R^3)}{r_i^3}\frac{\dot{R}^2}{2}\right) \tag{3.9}$$

Here, r_i is the source to receiver distance, and the term $(r_i^3 - R^3)/r_i^3$ will be neglected as in the far-field this term approaches zero when the bubble radius R is significantly smaller than the radius r_i, i.e $R \ll r_i$. The enthalpy H in an incompressible fluid can be approximated as (Gilmore, 1952):

$$H \approx \frac{p(t) - p_\infty}{\rho} \tag{3.10}$$

The pressure $p_n(t)$ is the notional source. The scattered $p(t)$ can be calculated using Eq. 3.2 by using the operating pressure p_o, initial radius R_0 and the modelled radius from Eq. 3.3.

3.2.1 Far-Field Signal

Accurate source signature estimation is important in seismic processing. In 1982, Ziolkowski proposed and developed a method of obtaining the source signature in an airgun array by assuming the pressure wavefield to be the superposition of individual airguns as monopole wavefields that are located at the position of their respective bubbles. Placing hydrophones under each airgun at a 1m distance can help determine the required measurements. This method was later developed by Parkes et al. (1984), who derived the recursive solution for this method.

$$p_f(t) = \sum_i \frac{s_i(t - r_i/c)}{r_i} + r\frac{s_i\left(t - r_i^g/c\right)}{r_i^g} \tag{3.11}$$

Here, $p_f(t)$ is the measured pressure signal as a cumulative response of the monopole sources, r_i is the distance from the far-field(observation point) to the bubble (i), r_i^g is the distance between projected far-field to the bubble for the source ghost, S_i is the notional source measurement for the source (i), c is the water velocity, and r is the reflection coefficient of the air-water interface (-1).

Chapter 4

Methodology

The bubble radius and velocity were modelled by solving the ordinary differential equations 3.1 - 3.8 using a numerical solver based on the Runge-Kutta (4,5) method that was readily available in MATLAB as the ode45 function. Equation 3.7 was solved using an adaptive time-stepping that was refined to the order 10 to avoid large time steps. The bubble is produced by the expulsion of air from the airgun into the surrounding water. The bubble at rest has zero velocity and expands with an initial radius that is defined using equation 3.3. The constants used for solving the equations are listed in table 4.1 with their description and values. The variable parameters were Reynolds number (Re) from Eq. 3.8 and the second differential of pressure from $\dot{p}$ Eq. 3.7. The modelling is performed at source depths below $d_{fs} = 3.8V_g^{1/3}$, where V_g is the volume of the airgun in a cubic inch. A condition-based modelling scheme was employed to obtain the corrected radius and pressure in the case of a bubble bursting and collapsing around the free surface. The analysis scheme finds the zones when the bubble touches the free surface, expands, breaks and finally collapses.

The modifications applied to the simple Rayleigh-Plesset modelling will capture the critical radius of the bubble (i.e. when the thin layer above the free surface ruptures). The process of modelling is done in two stages. The modelling terminates when the first oscillation is complete after which the initial radius and velocity are redefined. The ODE is run again and terminated after the elapsed time is equal to the two-way collapse time of the bubble. In this way, the resultant radius follows the bubble's surface displacement during breakage and collapse.

The modelled radius and velocity are used to get the pressure response of the bubble. Using Eq. 3.9 the far-field pressure without the ghost is found. This pressure is interpolated over a finer time grid and the ghost is iteratively added to the signal using Eq. 3.11. A Savitzky-Golay smoothing filter is applied to the frequency spectrum.

The modelling methodology explained above has been summarised in a flow chart in figure 4.1. The input variables for the ODE are initial velocity V_0 and initial radius R_0 of the oscillating bubble, while the output of the modelling

algorithm is the far-field signal at $r_i = 20$ m.

4.1 Modelling Approach

Recent studies have compared Gilmore and Rayleigh-Plesset equations for the modelling of explosion-type bubbles i.e minimum initial radius and pressure. For an initial radius greater than 100µm, the effect of surface tension and dynamic viscosity terms are considered to be negligible (Graaf et al., 2014). The difference between these equations is noticeable but not significant when the ratio between the initial pressure and hydrostatic pressure is higher than a factor of 10 (Graaf et al., 2014). Due to this reason, the acoustic pressure is modelled with the Rayleigh-Plesset Eq. 3.7.

Equations 3.1 to 3.8 model bubble oscillations for any source depth but they do not account for the bubble and free-surface interaction. The assumptions discussed above apply to a single spherical bubble in an infinite liquid. However, in the case of a bubble breaking at the free surface, new assumptions will be made in terms of; a) The density of gas inside the bubble, b) The change in pressure of the surrounding medium from water to air, and regarding c) Re-estimating the minimum radius of the bubble after bursting at the free surface.

The thickness of the water film around the bubble is assumed to be thin as the period between bubble expansion, bursting and collapse is in milliseconds. The initial pressure modelled using Eq. 3.2 is tracked by defining a condition-based modelling scheme that modifies the pressure to mimic the bubble bursting, and its subsequent reduction in gas volume. In the event of a bubble bursting at the free surface, the pressure inside the bubble will come to an equilibrium instantly as the gas inside the bubble escapes into the atmosphere. After this stage, the dynamic viscosity and medium density are modified. The dynamic viscosity value is changed from 0.01 Pa to 17.1 µPa (i.e. change of medium from water to air)(Koukouvinis et al., 2016). The bubble bursts after rising above the surface and so the density of the medium will be equivalent to the density of air which is found through the adiabatic equation of state given in Eq. 4.1 (T. Li et al., 2019).

$$\rho_{gas} = \rho \left(\frac{p_\infty}{p(t)} \right)^{1/\gamma} \tag{4.1}$$

From the time of the air bubble bursting until it starts contracting (i.e below the free surface), the polytropic index is taken as 1 for the isothermal case.

After bursting, the bubble's radius rapidly reduces in size and forms a second bubble that will oscillate with a much lower initial pressure inside the bubble. To accurately model this behaviour, the first stage of modelling terminates when the radius of the bubble is $R = z_s - R_o$ (i.e when the bubble is contracting after the critical radius is seen). The modelling then continues into the second stage with different initial conditions. In particular, The initial velocity is taken

as the last value from the first stage, but with a negative sign to propel the decrease in radius of the bubble. The initial radius is taken as $R_o = (z_s - R_o)/1.5$ which limits the maximum radius of the second bubble to source depth. In addition, the gas pressure inside the bubble is taken as the atmospheric pressure P_{atm} since there is no longer a thin layer separating the part of the bubble above the free surface and air.

The reflection coefficient was tested iteratively at varying source depths. Assuming a small difference in the density of gas inside the bubble and air, a reflection coefficient of r=-0.9 was chosen to model the far-field scattered pressure with its ghost at 0.1 m and 0.15 m source depths. The reflection coefficient calculated from Eq. 2.1 and Eq. 2.2 was much higher than what would be expected for a gas bubble bursting at the free surface. As the receiver is placed adjacent to the sources, inside the water column, a value of -0.9 for the reflection coefficient is selected.

Parameter	Description	Value
p_0	Operating pressure of the airgun	$137x10^5$ Pascal
V_g	Volume of the airgun	12 inch^3
R_o	Initial Radius of the bubble	0.0361
V_0	Initial Volume of the bubble	0
ρ_{inf}	Ambient density of water	1000 kg/m^3
P_{atm}	Atmospheric pressure	101320 Pascal
S	Surface tension of water	0.0728 N/m
c_{inf}	Ambient speed of sound in water	1450m/s
g	Gravitational acceleration constant	9.8 m/s^2
γ_a	polytropic constant for adiabatic case	1.13
γ_i	polytropic constant for isothermal case	1
ν_w	Dynamic viscosity constant for water	$1x10^{-3}$
ν_a	Dynamic viscosity constant for air	$1.71x10^{-5}$
d_r	Receiver depth in the water-tank experiment	0.5 m
d_{r_f}	Receiver depth in the far-field	0.5 m

Table 4.1: List of constants used for the Rayleigh-Plesset modelling and their descriptions.

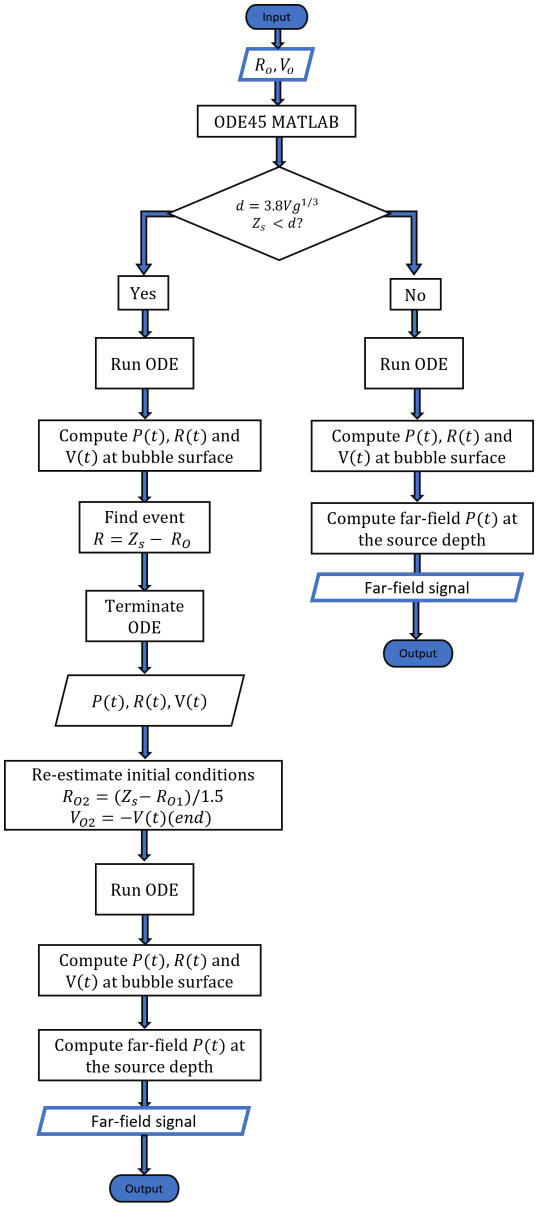

Figure 4.1: Flow diagram of the modelling scheme.

Chapter 5

Results and Discussion

5.1 Near and Far-field Pressure Response

Figure 5.1 shows the modelled radius that is used to model the pressure response at source depths 0.1 m and 0.15 m. Figure 5.4 compares the modelled pressure with the radius obtained from simple Rayleigh-Plesset modelling. R_{max} is achieved when the pressure response has a minimum. The modelled radius is similar to the radius of the initial bubble obtained from the numerical simulation of a single bubble bursting at the free surface in Koukouvinis et al. (2016). The pressure response of a bursting bubble fluctuates violently as the bubble collapses in figure 5.4.

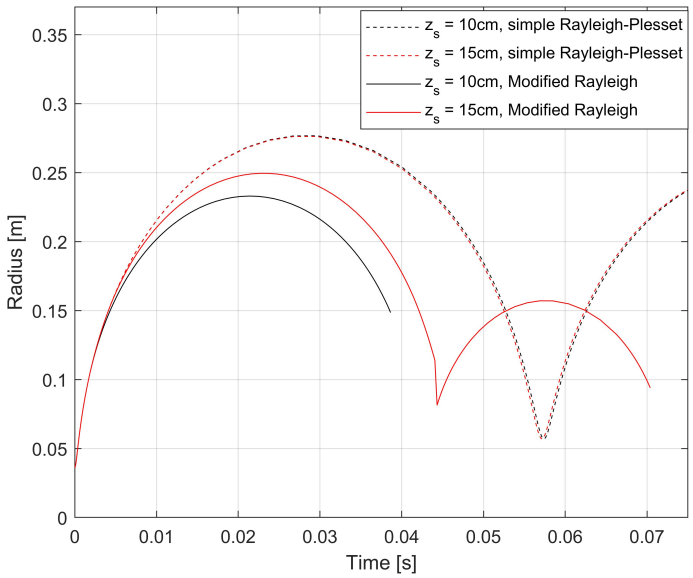

Figure 5.1: Modelled radius of 10 cm and 15 cm source signatures. Solid lines model the shift in the bubble period after the bubble and free surface interaction is taken into account.

The maximum radius R_{max} of the bubble is used to obtain the maximum displacement of the free surface as $d_{max} = R_{max} - z_s$. As seen in the recordings by Wehner (2019a), the bubble produced at 0.1 m source collapses after it bursts at the free surface, hence the radius was modelled until the collapse time as seen in figure 5.1. If the radius of 0.1 m source is modelled until the formation and collapse of the 'torus' of the bubble which is defined as the breaking of the bubble into two toroidal shapes when the jet produced by the collapsing bubble pierces through it, the acoustic pressure will include bubble energy after the first peak. Hence, the modelling of the 0.1 m source was terminated before the onset of the second oscillation.

As the recorded signal at the 0.15 m source contains bubble oscillation after the first peak, the radius modelling at the source depth was terminated before the onset of the third oscillation of the bubble. In this way, the recorded and modelled signals are comparable.

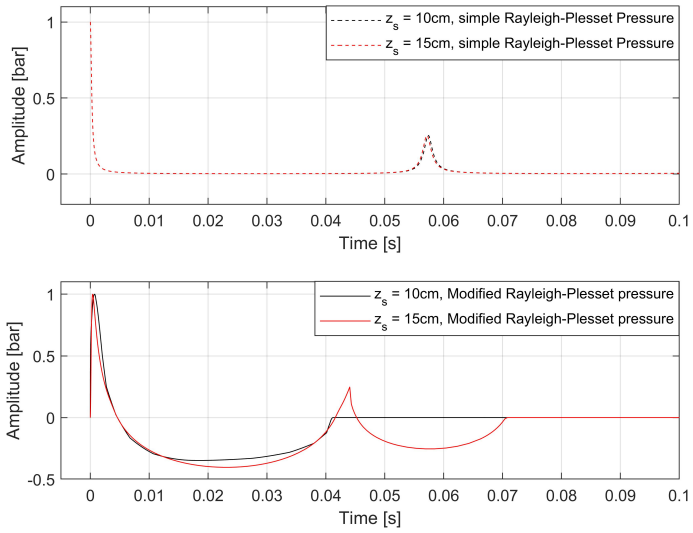

Figure 5.2: Modelled near-field pressure response of 10 cm and 15 cm source signatures using a simple and modified Rayleigh-Plesset modelling approach.

The pressure signals are normalised for comparison by dividing all values by the maximum pressure. The bubble peak is lower for the 0.15 m source compared to 0.1 m. The near-field signals in figure 5.2 are obtained at a receiver depth of 0.5 m using Eq. 3.9. The pressure response in figure 5.2 for simple and modified Rayleigh-Plesset modelling differs due to the modelled radius of the bubble.

Figure 5.4 shows the difference in peak and bubble amplitudes for the two signals. The pressure responses have similar peak amplitude and width with a comparable frequency response.

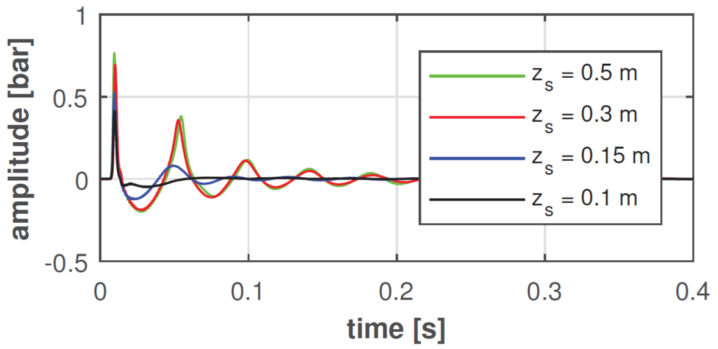

Figure 5.3: Pressure response at variable source depths recorded at H1 receiver fired from a 12 $inch^3$ source. Signals are corrected for geometrical spreading by multiplying with 1/r where r is the source-receiver distance (Wehner, 2019a)

By adding the source ghost scaled by the reflection coefficient of the free surface into the near-field signal, we obtain the far-field signals in figure 5.4. The modelled far-field signals for a receiver placed 20 m below the airgun obtained in figure 5.4 can be compared qualitatively with the recorded signals in figure 5.3. The period of the second oscillation for the modelled and recorded data is similar (∼0.06 ms) at 0.15 m source depth. The far-field signal with the source ghost is obtained from Eq. 3.11. With the addition of ghost in the far-field, the pressure response differs from the recorded signal. The source ghost dampens the bubble enrgy and increases the Peak-to-Bubble ratio from 4.5 to 23.8 at 0.15 m.

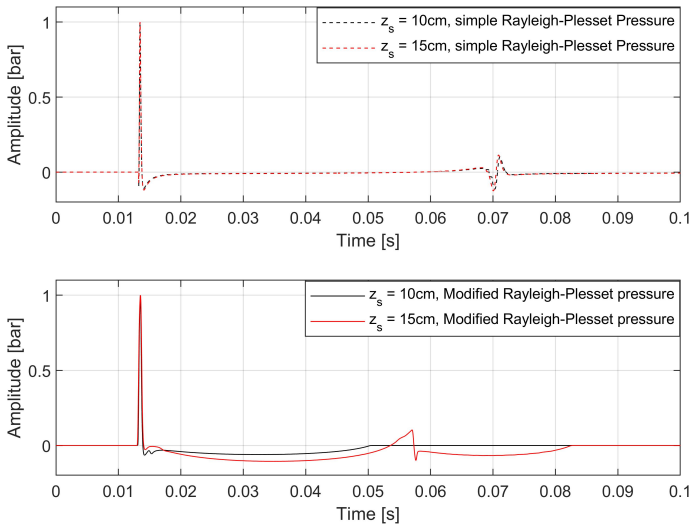

Figure 5.4: Modelled far-field pressure response of 10 cm and 15 cm source signatures using simple and modified Rayleigh-Plesset modelling approach. Solid lines model the reduced amplitude after bubble and free surface interaction is taken into account.

5.2 Comparison of shallow and deep signal

The modelled signals at 0.1 m and 0.15 m are compared with the recorded signal at 7.5 m source depth with their respective frequency spectra in figure 5.5. A Savitzky-Golay smoothing filter has been applied to the frequency spectra with weights $w = 3$ for 7.5 m and 0.1 m signals and $w = 5$ for 0.15 m signal. The filter slightly smooths out the notches in the frequency spectrum in figure 5.5. The shallow signals have higher amplitude at frequencies between 0-7 Hz for 0.1 m signal and 0-12 Hz for 0.15 m signal. The higher amplitude in the 7.5 m signal is due to the bubble oscillations which contribute to low frequencies, however, these bubble oscillations are removed by the process of de-bubbling.

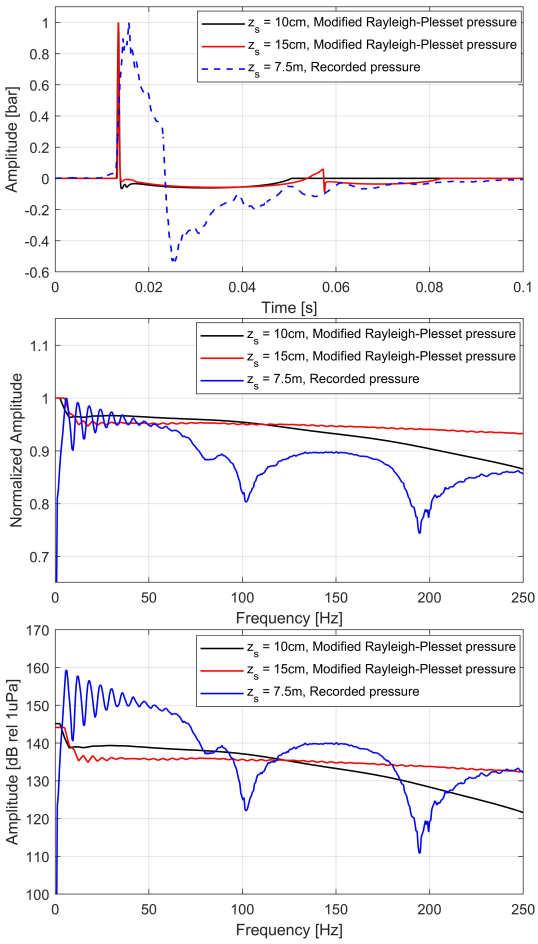

Figure 5.5: Modelled far-field pressure response at $r_i = 20m$ for sources placed at 10 cm and 15 cm ($V_g = 12$ inch^3, $p_0 = 137x10^5$ Pascal) compared to recorded far-field signal at $r_i = 80m$ for source placed at 7.5 m ($V_g = 400$ inch^3, $p_0 = 137x10^5$ Pascal)(top) with their respective frequency spectra (bottom). The relative normalised amplitude change of the frequency spectra is seen in the middle figure. Notice the reduced source ghost and bubble oscillations at 10 cm and 15 cm in the top figure.

5.3 Surface displacement

The surface displacement determined using Eq. 2.10 (h_{ch}) is compared to the difference between modelled maximum radius and the source depth (h_m) in table 5.1. Error percentage was determined by taking the difference between the two surface displacements, divided by the h_{ch}.

Source depth (z_s)	h_m	h_{ch}	% error
0.1 m	0.1330 m	0.1341 m	0.8%
0.15 m	0.0995 m	0.153 m	34%

Table 5.1: Percentage error between the recorded and modelled surface displacements.

The difference between the modelled h_m and recorded surface displacement h_{ch} is likely attributed to the modelling approach taken as discussed in the next section. The pressure response was modelled by solving the Rayleigh-Plesset ODE compared to other methods used to model the bubble and free surface interaction such as through CFD (computational fluid dynamics) simulations, and the inversion-based Kirkwood-Bethe (1942) equation. The equations described in chapter 3 consider the spatial change in radius compared to the simulation and inversion-based models. Numerical simulations of bubbles collapsing near a free surface describe the change in the shape of the bubble in detail. This behaviour is observed in simulation results presented by Boulton-Stone and Blake (1993) (figure 3) of a collapsing bubble near a free surface. This non-spherical deformation of the airgun bubble surface caused by its interaction with the free surface is also discussed in S. Li et al. (2020).

5.4 Primary Bjerknes Force

The primary Bjerknes force in figure 5.6 for the modelled bubble at 0.1 m sources is determined using Eq. 2.11. As the bubble expands, the Bjerknes force moves towards the anti-node of the pressure indicated by the left arrow, and as it interacts with the free surface the Bjerknes force moves towards the node of the pressure as indicated by the right arrow. Positive $\delta p(t)$ shows that the bubble is contracting, and vice versa. The value of $-V\delta p(t)$ starts to increase from the formation of the bubble until its collapse and decreases until there is no longer an acoustic pressure recorded at the hydrophone. The peak in figure 5.6 is the event of the bubble bursting at the free surface after which the bubble pressure reaches equilibrium around 0.04 s. The time of source ghost arrival for 0.1 m signal is ∼0.01 s. The additional acoustic energy after the bubble collapse needs to be investigated in figure 5.6.

The current modelling approach cannot model the jet formation after bubble bursting, however, numerical simulation-based studies have described the bubble jet velocity as stationary (Deike et al., 2018). Wehner (2019a) discussed the contrasting pressure recordings in water and air at shallow depths and associated the pressure recorded in the air with the conversion of evanescent waves in water into homogenous waves in air. The hydrophone placed above water records a peak and trough ∼0.02 s after the bubble bursts at the free surface at 0.1 m source depth. The signal in air records a positive pressure response

after the trough which can be a result of the jet stream forming both at the interface (outward) and bubble (inward) as simulated by T. Li et al. (2019). The simulated bubble bursting behaviours are characterized by the varying standoff parameter r_s i.e the distance between source and free surface r_i scaled by the maximum radius R_{max}. At 0.1 m source depth, the maximum radius of the modelled bubble is 0.233 m which gives a standoff parameter of $r_s = 0.43$. Taking into account the simulated pressure and bubble radius for $r_s = 0.5$ in T. Li et al. (2019), we observe an increase in pressure when the jet is released into the air, and simultaneously a decrease in pressure inside the bubble as it collapses. The coupling of an external force such as the jet velocity can be explained as the source of additional pressure response received at the hydrophone.

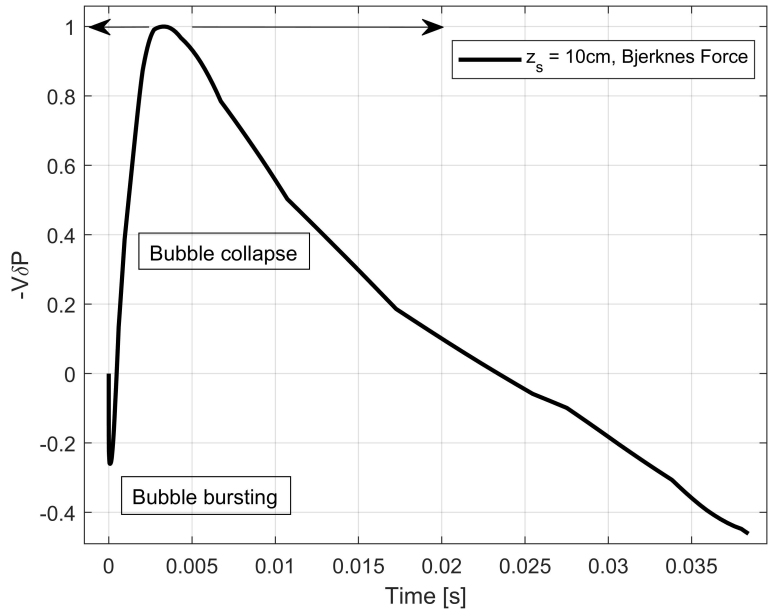

Figure 5.6: Primary Bjerknes force plotted against time for the bubble modelled at 0.1 m.

Chapter 6

Conclusion

The pressure response of a shallow seismic source was modelled using the Rayleigh-Plesset equation. In this modelling, the bubble was assumed to be expanding above the free surface during its first oscillation and this interaction was considered using a condition-based modelling scheme. The bubble was modelled in two stages to mimic the bursting and collapsing behaviour from its interaction with the free surface. The modelled pressure can be qualitatively compared to the recorded measurements at the source depths. The modelling of bubble radius is terminated before the onset of the second oscillation for 0.1 m source, and before the onset of the third oscillation for 0.15 m sources. The modelled data were compared to the recorded data in terms of Peak-to-Bubble ratio, bubble period and surface displacement. These error in modelled and estimated surface displacement is 0.8% for 0.1 m source depth and 34% for 0.15 m source depth. The comparison of recorded and modelled signals suggests a qualitative match. The frequency spectrum of the shallow source signals shows an addition of 6.6 dB from 0-7 Hz for 0.1 m source and 7.6 dB from 0-12 Hz for 0.15 m source signal. The normalized relative change in amplitude at shallow sources suggests an increase in amplitude at these frequencies compared to the normalized relative change in amplitude at a deeper 7.5 m source signal. Such signals will not need de-bubbling as the signal at 0.1 m is close to an ideal source signature, while the contribution towards the enhanced low-frequency spectra at 0.15 m is not from the bubble itself.

The modelling approach described in this thesis has its advantages and disadvantages. Compared to simulation or inversion-based modelling approaches, the error between the modelled and recorded pressure is likely to be higher. The numerical simulation-based studies mentioned in Chapter 1 have modelled the interaction of a bubble near a free surface using the Rayleigh-Plesset equation as well though the goal of these simulations is to find the parameters that affect the pressure response of the bubble such as viscosity, surface tension and temperature. By defining the bubble wall thickness and thermal convection across it as suggested by Graaf et al. (2014), the modelling approach presented in this thesis can be improved. Despite following a simple modelling approach,

the far-field acoustic pressure from very shallow sources can be predicted by the model presented in this thesis.

Bibliography

Amundsen, L. & Landro, M. (2014). Is it optimal to tow air guns shallow to enhance low frequencies? *Geophysics*, *79*(3). https://doi.org/10.1190/geo2013-0348.1

Amundsen, L., Westerdahl, H., Pedersen, Å. S., Thompson, M. & Landrø, M. (2017). On firing an air gun very shallow. *Geophysics*, *82*(3), A25–A29. https://doi.org/10.1190/geo2016-0617.1

Besant, W. (1859). *A treatise on hydrostatics and hydrodynamics*. Deighton, Bell. https://books.google.no/books?id=xzcDAAAAQAAJ

Boulton-Stone, J. M. & Blake, J. R. (1993). Gas bubbles bursting at a free surface. *Journal of Fluid Mechanics*, *254*, 437–466. https://doi.org/10.1017/S0022112093002216

Brennen, C. E. (2013). *Cavitation and bubble dynamics*. Cambridge: Cambridge University Press. https://doi.org/10.1017/CBO9781107338760

Cui, P., Zhang, A. M. & Wang, S. P. (2016). Small-charge underwater explosion bubble experiments under various boundary conditions. *Physics of Fluids*, *28*(11), 117103. https://doi.org/10.1063/1.4967700

Deike, L., Ghabache, E., Liger-Belair, G., Das, A., Zaleski, S., Popinet, S. & Séon, T. (2018). Dynamics of jets produced by bursting bubbles. *Physical Review Fluids*, *3*. https://doi.org/10.1103/PhysRevFluids.3.013603

Dragoset, B. (2005). A historical reflection on reflections. *The Leading Edge*, *24*(s1), s46–s70. https://doi.org/10.1190/1.2112392

Gilmore, F. (1952). *The growth or collapse of a spherical bubble in a viscous compressible liquid*. California Institute of Technology.

Graaf, K., Penesis, I. & Brandner, P. (2014). Modelling of seismic airgun bubble dynamics and pressure field using the gilmore equation with additional damping factors. *Ocean Engineering*, *76*, 32–39. https://doi.org/10.1016/j.oceaneng.2013.12.001

H. N., O. & A, P. (1990). Bubble oscillations in the vicinity of a nearly plane free surface. *The Journal of the Acoustical Society of America*, *85*(5), 2085–2092. https://doi.org/10.1121/1.399560

Haavik, K. (2016). *Source depth diversity for enhanced marine seismic imaging* (Thesis).

Hatton, L. (2007). An empirical relationship between surface reflection coefficient and source array amplitude. http://www.leshatton.org/anelastic_surface_reflection_coefficient.html

Hatton, L. & Parkes, G. (1986). *The marine seismic source*. Springer Dordrecht. https://doi.org/10.1007/978-94-017-3385-4

Hegna, S. & Parkes, G. (2012). The low frequency output of marine air-gun arrays. *Seg technical program expanded abstracts 2011* (pp. 77–81). https://doi.org/10.1190/1.3628192

Herring, C. (1941). *Theory of the pulsations of the gas bubble produced by an underwater explosion* (Report). Columbia University, Divison of National Defense Research.

Hoff, L. (2003). *Acoustic characterization of contrast agents for medical ultrasound imaging*. Kluwer Academic Publishers. https://doi.org/10.1016/S0301-5629(02)00646-4

Keller, J. B. & Kolodner, I. I. (1942). Damping of underwater explosion bubble oscillations. *Journal of Applied Physics*, *27*, 1152–1161.

Khodabandeloo, B. & Landrø, M. (2017). Effects of ghost cavitation cloud on near-field hydrophones measurements in the seismic air gun arrays. https://doi.org/10.3997/2214-4609.201700845

Kirkwood, J. G. & Bethe, H. A. (1942). *Shock and detonation waves* (Report). OSRD Report.

Koukouvinis, P., Gavaises, M., Supponen, O. & Farhat, M. (2016). Simulation of bubble expansion and collapse in the vicinity of a free surface. *Physics of Fluids*, *28*(5), 052103. https://doi.org/10.1063/1.4949354

Krieger, j. & Chahine, G. (2005). Acoustic signals of underwater explosions near surfaces. *The Journal of the Acoustical Society of America*, *118*, 2961–2974. https://doi.org/10.1121/1.2047147

Kryvohuz, M. & Campman, X. (2019). Prediction of signatures of airgun arrays using dual near-field hydrophones. *Geophysical Prospecting*, *67*. https://doi.org/10.1111/1365-2478.12754

Leighton, T., Walton, A. & Pickworth, M. (1989). Primary bjerknes forces. *European Journal of Physics*, *11*, 47. https://doi.org/10.1088/0143-0807/11/1/009

Li, S., van der Meer, D., Zhang, A.-M., Prosperetti, A. & Lohse, D. (2020). Modelling large scale airgun-bubble dynamics with highly non-spherical features. *International Journal of Multiphase Flow*, *122*, 103143. https://doi.org/10.1016/j.ijmultiphaseflow.2019.103143

Li, T., Zhang, A.-M., Wang, S.-P., Li, S. & Liu, W.-T. (2019). Bubble interactions and bursting behaviors near a free surface. *Physics of Fluids*, *31*(4), 042104. https://doi.org/10.1063/1.5088528

Long, A. (2021). Low-frequency marine seismic source considerations. *Industry Insights, PGS*.

Loo, S., Terwisga, T., Hoeijmakers, H. & Hoekstra, M. (2012). Numerical study on collapse of a cavitating cloud of bubbles, 227–239. https://doi.org/10.3850/978-981-07-2826-7_187

Loveridge, M. M. (1985). *Marine seismic source signatures, directivity and the ghost* (Thesis).

Mayne, W. H. & Quay, R. G. (1971). Seismic signatures of large air guns. *Geophysics*, *36*(6), 1162–1173. https://doi.org/10.1190/1.1440237

PGS. (2017). *Marine vibrators get closer to reality*. Retrieved December 13, 2017, from https://www.pgs.com/publications/feature-stories/marine-vibrators

Plesset, M. S. & Prosperetti, A. (1977). Bubble dynamics and cavitation. *Annual Review of Fluid Mechanics*, *9*(1), 145–185. https://doi.org/10.1146/annurev.fl.09.010177.001045

Plesset, M. (1949). The dynamics of cavitation bubbles. *Journal of Applied Mechanics*, *16*, 277–282.

Rayleigh, O. (1917). On the pressure developed in a liquid during the collapse of a spherical cavity. *Philosophical Magazine Series*, *6*(200), 94–98.

Robinson, P. B., Blake, J. R., Kodama, T., Shima, A. & Tomita, Y. (2001). Interaction of cavitation bubbles with a free surface. *Journal of Applied Physics*, *89*(12), 8225–8237. https://doi.org/10.1063/1.1368163

Sanders, J. I. & Barr, F. J. (1989). Attenuation of water-column reverberations using pressure and velocity detectors in a water-bottom cable. *SEG Technical Program Expanded Abstracts*, 653–656. https://doi.org/10.1190/1.1889557

Sheriff, R. (2002). *Encyclopedic dictionary of applied geophysics*. Society of Exploration Geophysicists.

U.S. Environmental Protection Agency, E. (2016). *Marine seismic methods*. Retrieved May 18, 2016, from https://archive.epa.gov/esd/archive-geophysics/web/html/marine_seismic_methods.html

Vokurka, K. (1986). Comparison of rayleigh's, herring's, and gilmore's models of gas bubbles. *Acta Acustica united with Acustica*, *59*.

Wehner, D. (2019). *Experimental studies of the acoustic signal generated by marine seismic sources* (Thesis).

Wehner Daniel, L. M. & Lasse, A. (2019). The impact on low frequencies from very shallow air guns in marine seismic acquisition - an experimental study. *Geophysics*, *84*, 61. https://doi.org/10.1190/geo2018-0687.1

Weston, D. (1960). Underwater Explosions as Acoustic Sources. *Proceedings of the Physical Society*, *76*(2), 233–249. https://doi.org/10.1088/0370-1328/76/2/307

Willis, H. (1941). *Underwater explosions, time interval between successive explosions.* (Report). Royal Naval Scientific Service.

Zhou, H. & Amundsen, L. (2013). Low-frequency seismic deghosting. *Geophysics*, *78*, WA15–WA20.

Ziolkowski, A. (1970). A Method for Calculating the Output Pressure Waveform from an Air Gun. *Geophysical Journal International*, *21*(2), 137–161. https://doi.org/10.1111/j.1365-246X.1970.tb01773.x